Article

Topological Model of Spatial Connectivity: Geometric Anisotropy from G_{ik} and Cosmological Consequences of Variable c_{eff}

Konstantin Budrin *

Posted Date: 24 October 2025

doi: 10.20944/preprints202510.1813.v1

Keywords: topological field theory; geometric unification; spatial connectivity; anisotropy of metric; variable speed of light; cosmology of early universe

 doi:10.20944/preprints202510.1813.v1

Article

Topological Model of Spatial Connectivity: Geometric Anisotropy from G_{ik} and Cosmological Consequences of Variable c_{eff}

Konstantin Budrin

Independent Researcher, Montenegro; kbudrin@gmail.com

Abstract

Since the early twentieth century, the quest to describe all fundamental interactions as manifestations of a single geometric structure of spacetime has remained central to theoretical physics. Einstein's unified–field program attempted to generalize gravity by including electromagnetism on a geometric basis, and later developments—from Kaluza–Klein models to modern string theory and loop quantum gravity—have continued this line of thought. Yet the reconciliation of general relativity (GR) and quantum mechanics (QM) is still incomplete: GR captures macroscopic curvature but neglects quantum discreteness, while QM relies on a fixed background. Here we propose a minimal geometric framework in which space is characterized by *local topological connectivity* defined by a universal constant ℓ_*, the *fundamental connectivity length*. This constant represents the smallest invariant separation between neighboring points of space and serves as the microscopic carrier of geometric information. Local anisotropies of the spatial metric G_{ik} stretch or compress this invariant unit, giving rise to an *effective Planck length*

$$L_p(x,\hat{n}) = \ell_* \sqrt{G_{ik}(x)\,\hat{n}^i\hat{n}^k},$$

and to the corresponding *effective speed of light*

$$c_{\text{eff}}(x) = \left(\frac{\hbar G}{[L_p(x)]^2}\right)^{1/3}.$$

In the isotropic limit $G_{ik} \to \delta_{ik}$ one recovers $L_p = \ell_* = \ell_p$ and $c_{\text{eff}} = c_0$, ensuring full compatibility with local Lorentz invariance. Variations of $G_{ik}(t)$ then induce the apparent evolution of $L_p(t)$ and $c_{\text{eff}}(t)$, producing a natural early–universe regime where $L_p \to 0$ and $c_{\text{eff}} \to \infty$. This mechanism removes the cosmological horizon problem without requiring an inflationary potential and regularizes curvature singularities by introducing a finite topological cutoff ℓ_*. The construction unifies the geometric content of electromagnetism and gravitation through the symmetric and antisymmetric parts of the local tensor G_{ik}, reproducing the Einstein–Maxwell equations in the quasi–isotropic limit. It further allows a topological interpretation of elementary particles as stable connectivity defects (torus for the electron, trefoil for the proton, balanced knot for the neutron). Observable consequences include direction–dependent gravitational lensing, polarization–dependent propagation of gravitational waves, and potential anisotropic signatures in the cosmic microwave background and the stochastic gravitational–wave background. The proposed framework preserves mathematical minimalism—a single additional constant ℓ_*—while yielding falsifiable predictions that can be tested with current and forthcoming observational data.

Keywords: topological field theory; geometric unification; spatial connectivity; anisotropy of metric; variable speed of light; cosmology of early universe

 doi:10.20944/preprints202510.1813.v1

Contents

1. Introduction

The unification of quantum mechanics (QM) and general relativity (GR) remains one of the central unresolved problems of fundamental physics. Beginning with Einstein's works, numerous attempts have been made to construct a single geometric picture of interactions. However, the known approaches—from classical Kaluza–Klein models to modern string theory [1] and loop quantum

 doi:10.20944/preprints202510.1813.v1

gravity (LQG) [2,3]—face a number of difficulties. String theories require additional dimensions and an enormous multiplicity of modes, whereas LQG relies on a discretization of geometry but has not yet produced a self-consistent phenomenology. A common limitation of both directions is the scarcity of testable predictions that go beyond already established observations.

At the same time, within classical GR singularities inevitably arise—black holes, the cosmological singularity—which signal an incompleteness of the theory. The nature of elementary particles also remains geometrically unexplained: the Standard Model successfully describes their interactions but does not provide a geometric interpretation of mass or charge. Topological approaches, from Skyrme's solitons to modern models of cosmic strings, demonstrate the fruitfulness of topological reasoning but typically require complicated Lagrangians and auxiliary fields.

In this work, we propose an alternative route: to describe space not as a continuous four-dimensional manifold but as a locally connected three-dimensional structure characterized by a single fundamental constant ℓ_*—the *fundamental connectivity length*. Time, in such a picture, emerges as a counter of local connectivity updates. On the basis of three simple postulates we formulate a unified geometric field theory in which:

- global coordinate transformations are absent, and geometry is defined strictly locally;
- a fundamental invariant is preserved under infinitesimal displacements and rotations;
- a universal connectivity constant ℓ_* sets the minimal geometric scale, while local anisotropies are encoded solely in the tensor G_{ik}.

The interest of this model lies in its minimalism: only one new scale is introduced—ℓ_*, directly tied to curvature and topology. From it there naturally follow:

- regularization of singularities (for instance, the Kerr ring singularity is replaced by a minimal radius $r_{\min} \sim (R_S \ell_*^2)^{1/3}$);
- a topological interpretation of elementary particles as stable connectivity defects (electron—a torus, proton/neutron—a trefoil-type knot);
- modifications of cosmological distances while preserving local Lorentz invariance;
- astrophysically testable effects: photon rings and black-hole shadows (EHT), spectroscopy of gravitational-wave ringdown (LIGO/Virgo/KAGRA, LISA), pulsar-timing-array signals (PTA), and weak lensing (Euclid, SKA).

Thus, the proposed framework retains a strictly geometric basis, introduces only one new constant, and yields a broad spectrum of observable consequences, making it a promising target for near-future empirical tests.

The motivation for treating spatial connectivity as a single geometric structure has both historical and conceptual roots. Early speculative works in the mid-twentieth century (unpublished family manuscripts) suggested that all fields might arise from a single locally invariant geometry. The present formulation retains this principle of locality while expressing it in modern differential-geometric language and linking it directly to current cosmological and quantum-gravitational phenomenology.

2. Axioms of the Model

The construction is based on three minimal postulates that specify how local spatial connectivity, metric structure, and the fundamental scale ℓ_* determine all geometric and physical quantities. Together they establish the operational rules by which curvature, anisotropy, and field dynamics emerge from a single underlying connectivity principle.

Axiom 1 (Local invariant). For small spatial displacements and rotations, the scalar

$$I \equiv \sqrt{G_{ik} X^i Y^k}, \tag{1}$$

is preserved, where X^i, Y^k are infinitesimal local coordinate displacements on the three–dimensional connectivity domain and G_{ik} is the local metric tensor defined on Σ_t. This expresses the invariance

 doi:10.20944/preprints202510.1813.v1

of the local scalar product under infinitesimal transformations, generalizing the preservation of $X\cdot Y$ in Euclidean space. The tensor G_{ik} is assumed C^2–smooth on scales $\gtrsim \ell_*$ so that finite differences admit a well–defined continuum limit. Its symmetric part S_{ik} determines the local spatial metric (curvature), while the antisymmetric part A_{ik} represents the infinitesimal *twist of connectivity* (a torsion–like component) that couples neighboring directions. In the isotropic limit $A_{ik}\to 0$, the invariant (1) reduces to the Euclidean norm $\sqrt{\delta_{ik}X^iY^k}$.

Axiom 2 (Locality of geometry). Global coordinate transformations are absent in the general case; geometry is defined strictly locally within each connectivity region. All physical quantities are expressed through local tensors and their derivatives on this region. Derivatives are taken with respect to the Levi–Civita connection of the local four–metric $g_{\mu\nu}$ built from the 3+1 form (5) in a Gaussian chart ($g_{0i}=0$). Comparisons between neighboring regions use only data on their overlap; no global chart is assumed. All fields are C^2 on scales $\gtrsim \ell_*$ so that coarse–grained derivatives are well defined.

Axiom 3 (Fundamental connectivity scale). Space possesses a universal constant ℓ_*—the *fundamental connectivity length*—which sets the minimal topological separation between neighboring points. Local anisotropies and metric deformations encoded in G_{ik} rescale this invariant unit, giving the *effective Planck length*

$$L_p(x,\hat{n}) = \ell_* \sqrt{G_{ik}(x)\,\hat{n}^i\hat{n}^k}, \tag{2}$$

and the corresponding *effective speed of light*

$$c_{\text{eff}}(x) = \left(\frac{\hbar\, G}{[L_p(x)]^2}\right)^{1/3}. \tag{3}$$

In the isotropic limit $G_{ik}\to\delta_{ik}$ one recovers $L_p=\ell_*=\ell_p$ and $c_{\text{eff}}=c_0$. Thus, ℓ_* is a fixed fundamental constant, while apparent variations of L_p and c_{eff} reflect geometric anisotropies rather than changes of physical constants.

Locally, the operational light speed c_{loc} entering (5) is constant (special relativity holds in each small neighborhood), whereas c_{eff} characterizes large–scale signal propagation that depends on G_{ik} and does not affect local Lorentz invariance. The tensor G_{ik} is a *dynamical* field of the theory; ℓ_*, $\hbar$, and G are constants. Calibration at the present epoch t_0 fixes $L_p(t_0)=\ell_p$ and $c_{\text{eff}}(t_0)=c_0$.

Operational remarks. (i) L_p is inferred from the response of local rods and clocks built from matter, hence depends on G_{ik} via (2); (ii) c_{eff} enters only in global observables (horizons, cosmography, lensing integrals) and reduces to c_{loc} in the quasi–isotropic limit; (iii) all small–scale statements are meaningful after coarse–graining on scales $\gtrsim \ell_*$.

3. Mathematical Basis

3.1. Emergent Time and Local Slicing

Consider a three–dimensional space endowed with local connectivity: two points are regarded as neighbors if their spatial separation is smaller than the fundamental length ℓ_*. The microscopic dynamics can be imagined as a sequence of *connectivity updates*, discrete steps $N\mapsto N+1$ in which the adjacency relations between neighboring points are renewed.

Definition of local time.

We introduce an *emergent* time coordinate as a counter of these steps:

$$t \;=\; N\,\Delta t, \qquad \Delta t \;=\; \alpha\,\frac{\ell_*}{c_{\text{loc}}}, \tag{4}$$

 doi:10.20944/preprints202510.1813.v1

where c_{loc} is the locally measured speed of light and $\alpha \sim \mathcal{O}(1)$ depends on the choice of gauge for the step size. In the limit of very frequent reconstructions ($\Delta t \to 0$ at fixed ℓ_*), time becomes continuous and ordinary derivatives appear as limits of finite differences:

$$\partial_t f \equiv \lim_{\Delta t \to 0} \frac{f(N+1) - f(N)}{\Delta t}.$$

3+1 representation.

Each instant t corresponds to a spatial hypersurface Σ_t with metric $G_{ik}(x,t)$. In local Gaussian coordinates ($g_{0i} = 0$) the four–metric reads

$$g_{\mu\nu}(x,t) = \begin{pmatrix} -c_{\mathrm{loc}}^2 & 0 \\ 0 & G_{ik}(x,t) \end{pmatrix}, \tag{5}$$

which is the standard 3+1 decomposition without shift. All covariant quantities below are defined with respect to $g_{\mu\nu}$; local Lorentz invariance is therefore maintained by construction.

3.2. Decomposition of the Local Tensor G_{ik}

Any rank–two tensor on Σ_t decomposes into symmetric and antisymmetric parts:

$$G_{ik} = S_{ik} + A_{ik}, \qquad S_{ik} = \tfrac{1}{2}(G_{ik} + G_{ki}), \quad A_{ik} = \tfrac{1}{2}(G_{ik} - G_{ki}). \tag{6}$$

The symmetric part S_{ik} represents the local spatial metric (gravitational geometry), while the antisymmetric part A_{ik} describes the local *twist of connectivity*, which will later appear as the spatial component of the antisymmetric field tensor F_{ij}.

3.3. From Local Phase Connectivity to the Four–Potential

Let a scalar *phase* function $\phi(x,t)$ be defined on Σ_t, whose gradient encodes the local linkage between neighboring points.[1] Define

$$\mathbf{A}(x,t) = \nabla\phi(x,t), \qquad \Phi(x,t) = -\,\partial_t\phi(x,t), \tag{7}$$

which are invariant under the gauge shift $\phi \mapsto \phi + \text{const}$. Combining them gives the four–potential (using c_{loc}=1 for simplicity[2]):

$$A_\mu = (\Phi,\, -A_i), \qquad A^\mu = (\Phi,\, A^i), \tag{8}$$

with indices raised and lowered by the metric (5).

3.4. Antisymmetric Part and the Field Tensor $F_{\mu\nu}$

Define the usual antisymmetric field tensor

$$F_{\mu\nu} = \nabla_\mu A_\nu - \nabla_\nu A_\mu = (\mathrm{d}A)_{\mu\nu}. \tag{9}$$

In local coordinates with $g_{0i} = 0$:

$$F_{0i} = E_i, \qquad F_{ij} = \epsilon_{ijk} B^k, \qquad \mathbf{E} = -\nabla\Phi - \partial_t \mathbf{A}, \quad \mathbf{B} = \nabla \times \mathbf{A}. \tag{10}$$

[1] When a small loop is traversed, the phase may accumulate an integer winding; this winding number characterizes a topological defect.

[2] In SI units the factors of c_{loc} are restored through $\varepsilon_0\mu_0 = 1/c_{\mathrm{loc}}^2$.

 doi:10.20944/preprints202510.1813.v1

Connection to A_{ik}.

At the geometric cutoff scale ℓ_* the antisymmetric component A_{ij} reproduces the spatial field tensor up to corrections of order ℓ_*^2:

$$A_{ij} = F_{ij} + \mathcal{O}(\ell_*^2), \tag{11}$$

i.e. A_{ij} is the geometric carrier of the local twist, whereas F_{ij} is its field representation. In the isotropic limit $G_{ik} \to \delta_{ik}$ the corrections vanish.

3.5. Bianchi Identities (Homogeneous Maxwell Equations)

From (9) and $d^2 = 0$ follows the Bianchi identity

$$\nabla_{[\alpha} F_{\beta\gamma]} = 0 \quad \Longleftrightarrow \quad \partial_\alpha F_{\beta\gamma} + \partial_\beta F_{\gamma\alpha} + \partial_\gamma F_{\alpha\beta} = 0, \tag{12}$$

which in three–vector form reads

$$\nabla \cdot \mathbf{B} = 0, \qquad \nabla \times \mathbf{E} + \partial_t \mathbf{B} = 0.$$

These are the homogeneous Maxwell equations—absence of magnetic monopoles and Faraday's induction law.

3.6. Sources as Topological Winding Defects

Phase winding along a small loop $\gamma \subset \Sigma_t$ is quantized:

$$\frac{1}{2\pi} \oint_\gamma \partial_s \phi \, ds = n \in \mathbb{Z}. \tag{13}$$

The worldlines of such defects $x_a^\mu(\tau)$ define the conserved four–current

$$J^\mu(x) = e \sum_a n_a \int d\tau \, \frac{dx_a^\mu}{d\tau} \, \delta^{(4)}\big(x - x_a(\tau)\big), \qquad \partial_\mu J^\mu = 0, \tag{14}$$

where charge conservation $\partial_\mu J^\mu = 0$ follows from the gauge symmetry $A_\mu \mapsto A_\mu + \partial_\mu \lambda$.

3.7. Variational Derivation of Inhomogeneous Maxwell Equations

The electromagnetic action (in SI units with $\varepsilon_0 \mu_0 = 1/c_{\text{loc}}^2$) is

$$S[A_\mu; J^\mu] = \int d^4x \, \sqrt{-g} \Big(-\frac{1}{4\mu_0} F_{\mu\nu} F^{\mu\nu} - J_\mu A^\mu \Big). \tag{15}$$

Variation with respect to A_ν using $\delta F_{\mu\nu} = \nabla_\mu \delta A_\nu - \nabla_\nu \delta A_\mu$ and integration by parts yield the Euler–Lagrange equations

$$\boxed{\nabla_\mu F^{\mu\nu} = \mu_0 \, J^\nu.} \tag{16}$$

Together with (12) these form the complete Maxwell system.

3.8. Field Energy and Relation to Curvature

Variation of the field action with respect to the metric gives the electromagnetic stress–energy tensor

$$T_{\mu\nu}^{(\text{EM})} = \frac{1}{\mu_0} \Big(F_{\mu\alpha} F_\nu{}^\alpha - \tfrac{1}{4} g_{\mu\nu} F_{\alpha\beta} F^{\alpha\beta} \Big). \tag{17}$$

The gravitational dynamics of the geometry is governed by

$$\boxed{R_{\mu\nu} - \tfrac{1}{2} g_{\mu\nu} R = \frac{8\pi G}{c_{\text{loc}}^4} \, T_{\mu\nu},} \tag{18}$$

 doi:10.20944/preprints202510.1813.v1

where $T_{\mu\nu}$ includes the electromagnetic contribution (17). In the local frame (5) these reduce to the usual Einstein equations with local c_{loc}.

3.9. Geometric Interpretation of the Field

At the microscopic scale ℓ_* the antisymmetric part A_{ik} of the connectivity tensor encodes the geometric twist of space. There exists a one–form $A = A_i\,dx^i$ such that, under smoothness at this scale,

$$A_{ij} = \partial_i A_j - \partial_j A_i + \mathcal{O}(\ell_*^2) = F_{ij} + \mathcal{O}(\ell_*^2). \tag{19}$$

Hence the electromagnetic field provides an *effective* continuum description of this geometric antisymmetry. In the isotropic limit and for curvatures small compared to ℓ_*^{-2}, the corrections vanish and standard electrodynamics on the background metric $g_{\mu\nu}$ is recovered.

Role of c_{loc} and global effects.

Locally c_{loc} is a postulated constant: all physical experiments within a sufficiently small neighborhood obey special relativity. Globally, however, the *effective* propagation speed of signals may vary through the geometry—for instance, via the metric–dependent scale $L_p(x)$ and the associated $c_{\mathrm{eff}}(x)$—without any violation of local Lorentz invariance. Such large–scale effects (e.g., in lensing or cosmography) are discussed in the applications and do not influence the local derivations in (16)–(18).

3.10. Quantum Mechanics as a Limit of Coarse–Graining at the Fundamental Scale ℓ_*; Classical Regime for Small Invariants

Step 0: Emergent time and 3+1 decomposition.

Time arises as a counter of connectivity updates with fixed step $\Delta t = \alpha\,\ell_*/c_{\mathrm{loc}}$ (see §3.1), which yields the continuous limit ∂_t. Locally we choose Gaussian coordinates ($g_{0i} = 0$), so that $g_{\mu\nu} = \mathrm{diag}(-c_{\mathrm{loc}}^2,\, G_{ik})$.

Step 1: Hydrodynamic variables.

For an ensemble of microscopic configurations we introduce the density $\rho(x,t) \geq 0$ and phase $S(x,t)$. In the presence of $A_\mu = (\Phi, -\mathbf{A})$ the velocity field is

$$\mathbf{v}(x,t) = \frac{1}{m}\big(\nabla S - q\mathbf{A}\big), \qquad \partial_t \rho + \nabla\cdot(\rho\,\mathbf{v}) = 0, \tag{20}$$

which is the local continuity equation.

Step 2: Hamilton–Jacobi equation and quantum correction.

The classical Hamilton–Jacobi (HJ) equation for S reads

$$\partial_t S + \frac{(\nabla S - q\mathbf{A})^2}{2m} + q\Phi + U(x,t) = 0. \tag{21}$$

Averaging, or coarse–graining, over fluctuations of the connectivity structure on the scale ℓ_* introduces an additional informational term, proportional to the local Fisher information density.[3] The result is the modified HJ equation

$$\partial_t S + \frac{(\nabla S - q\mathbf{A})^2}{2m} + q\Phi + U - \frac{\hbar^2}{2m}\,\frac{\nabla^2\sqrt{\rho}}{\sqrt{\rho}} = 0, \tag{22}$$

where the last term represents the *quantum potential*. Its appearance signals that the coarse–grained dynamics at the fixed geometric cutoff ℓ_* reproduces quantum behaviour.

[3] See, e.g., Reginatto (1998) and Hall & Reginatto (2002) for the derivation of the quantum potential from the Fisher scalar.

 doi:10.20944/preprints202510.1813.v1

Step 3: Passage to the Schrödinger equation.

Introducing the complex field $\psi = \sqrt{\rho}\,\exp(iS/\hbar)$, the system (20)–(22) is equivalent to the Schrödinger equation

$$\boxed{i\hbar\,\partial_t\psi = \left[\tfrac{1}{2m}\,(-i\hbar\nabla - q\mathbf{A})^2 + q\Phi + U(x,t)\right]\psi.} \tag{23}$$

Thus, standard quantum mechanics emerges as the hydrodynamic limit of a locally connected geometry when coarse–grained over the fundamental scale ℓ_*.

Classical regime.

Define characteristic variation lengths $L_\rho \sim \rho/|\nabla\rho|$, $L_A \sim |\mathbf{A}|/|\nabla\mathbf{A}|$, and $L_U \sim |U|/|\nabla U|$, and the dimensionless invariants

$$\varepsilon_\rho = (\ell_*/L_\rho)^2, \qquad \varepsilon_A = (\ell_*/L_A)^2, \qquad \varepsilon_U = (\ell_*/L_U)^2.$$

The classical limit corresponds to $\varepsilon_\rho, \varepsilon_A, \varepsilon_U \ll 1$, in which the quantum potential becomes negligible and Eq. (22) reduces to the classical Hamilton–Jacobi equation (21).

Classical regime: small invariants ℓ_*/L.

Let $L_\rho \sim \rho/|\nabla\rho|$ be the characteristic length of density variation, $L_A \sim |\mathbf{A}|/|\nabla\mathbf{A}|$, $L_U \sim |U|/|\nabla U|$, and the curvature radius $L_\mathcal{R}$ be defined by $|\mathcal{R}| \sim L_\mathcal{R}^{-2}$. Introduce the dimensionless invariants

$$\varepsilon_\rho = \left(\frac{\ell_*}{L_\rho}\right)^2, \qquad \varepsilon_A = \left(\frac{\ell_*}{L_A}\right)^2, \qquad \varepsilon_U = \left(\frac{\ell_*}{L_U}\right)^2, \qquad \varepsilon_\mathcal{R} = |\mathcal{R}|\,\ell_*^2.$$

The *classical regime* corresponds to

$$\varepsilon_\rho,\ \varepsilon_A,\ \varepsilon_U,\ \varepsilon_\mathcal{R} \ \ll\ 1,$$

in which the quantum potential $Q[\rho] = -\frac{\hbar^2}{2m}\frac{\nabla^2\sqrt{\rho}}{\sqrt{\rho}}$ is small compared with kinetic and potential energies, and Eq. (22) reduces to the classical Hamilton–Jacobi equation (21).

Predictable deviations from standard QM.

The finite and possibly anisotropic geometric scale ℓ_* leads to higher–order corrections that are suppressed by the small invariants defined above:

$$i\hbar\,\partial_t\psi = \left[\frac{1}{2m}(-i\hbar\nabla - q\mathbf{A})^2 + q\Phi + U\right]\psi + \gamma\,\ell_*^2(\mathbf{D}^2)^2\psi + \psi\,V_{\text{aniso}}[\rho;\beta^{ij}] + \frac{\hbar^2}{2m}\,\xi\,\mathcal{R}\,\psi + \cdots, \tag{24}$$

where $\mathbf{D} = \nabla - i\frac{q}{\hbar}\mathbf{A}$, β^{ij} is a small trace–free anisotropy tensor, and $\gamma, \xi = \mathcal{O}(1)$. The first correction term produces weak high–frequency dispersion $\propto \ell_*^2$, the second encodes directional effects arising from anisotropy of G_{ik}, and the third represents a geometric coupling to the scalar curvature $\mathcal{R}$. All such terms vanish in the quasi–isotropic limit $\varepsilon_\rho, \varepsilon_A, \varepsilon_U, \varepsilon_\mathcal{R} \to 0$, where $L_p \to \ell_*$ and standard quantum mechanics is recovered.

3.11. Anisotropic Regime

Anisotropy of the metric tensor G_{ik} leads to a directional dependence of observables (lensing, propagation of tensor modes, and related effects). Figure 1 schematically illustrates the distribution of anisotropy of the effective Planck scale $L_p(x,\hat{n}) = \ell_*\sqrt{G_{ik}\hat{n}^i\hat{n}^k}$.

 doi:10.20944/preprints202510.1813.v1

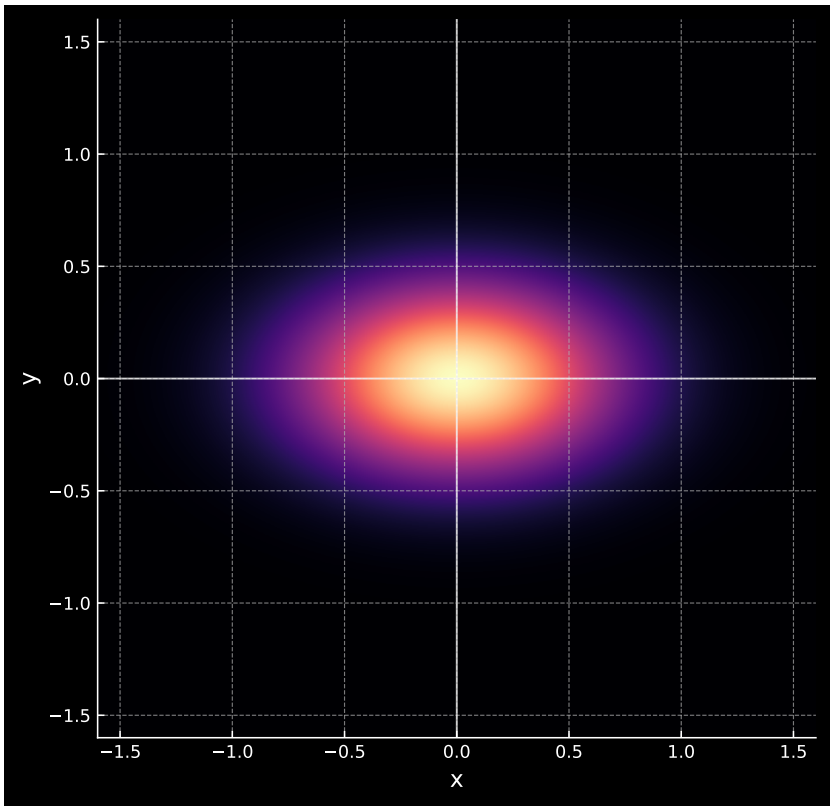

Figure 1. Schematic representation of anisotropy of the effective Planck scale L_p through the tensor G_{ik}.

4. Cosmology with Geometry–Dependent L_p and c_{eff}

4.1. Setup and Calibration

The fundamental constant ℓ_* is fixed once and for all. However, the local effective Planck length

$$L_p(t, \hat{n}) = \ell_* \sqrt{G_{ik}(t)\, \hat{n}^i \hat{n}^k}$$

and the corresponding signal speed

$$c_{\text{eff}}(t) = \left(\frac{\hbar G}{[L_p(t)]^2} \right)^{1/3}$$

may vary with the evolution of the metric tensor $G_{ik}(t)$. Calibration at the present epoch t_0 fixes $L_p(t_0) = \ell_p$ and $c_{\text{eff}}(t_0) = c_0$.

The slow, adiabatic evolution of $G_{ik}(t)$ ensures that local Lorentz invariance and the causal structure within each neighborhood are preserved at every epoch, while only the large–scale signal cone defined by $c_{\text{eff}}(t)$ changes in time.

4.2. Modified Friedmann Equations

For a spatially homogeneous and isotropic geometry the line element can be written as

$$ds^2 = c_{\text{eff}}(t)^2 dt^2 - a(t)^2 d\Sigma_k^2,$$

 doi:10.20944/preprints202510.1813.v1

where $d\Sigma_k^2$ is the metric of constant spatial curvature k. Treating $c_{\rm eff}(t)$ as the operational signal speed that sets the causal structure, the Einstein equations take the form

$$\left(\frac{\dot{a}}{a}\right)^2 = \frac{8\pi G}{3}\rho - \frac{k\,c_{\rm eff}(t)^2}{a^2} + \frac{\Lambda\,c_{\rm eff}(t)^2}{3}, \tag{25}$$

$$\frac{\ddot{a}}{a} = -\frac{4\pi G}{3}\left(\rho + \frac{3p}{c_{\rm eff}(t)^2}\right) + \frac{\Lambda\,c_{\rm eff}(t)^2}{3}. \tag{26}$$

The *operational* horizon distance is then

$$d_H(t) = a(t)\int_0^t \frac{c_{\rm eff}(t')}{a(t')}dt', \tag{27}$$

which measures the maximum comoving separation over which causal contact is possible.

Energy conservation in this framework follows from the covariant identity $\nabla_\mu T^{\mu\nu} = 0$, which yields the modified continuity equation

$$\dot{\rho} + 3H\left(\rho + \frac{p}{c_{\rm eff}^2}\right) = -\,\rho\,\frac{\dot{c}_{\rm eff}}{c_{\rm eff}}. \tag{28}$$

The right–hand side represents the geometric exchange of energy between matter and the varying causal structure: when $c_{\rm eff}$ decreases, part of the total energy density is effectively transferred into the background geometry.

If at an early epoch the metric anisotropy causes $L_p(t) \to 0$ and hence, by Eq. (3), $c_{\rm eff}(t) \to \infty$, the integral (27) becomes large even without an inflationary phase, thereby naturally resolving the horizon problem. The same mechanism also regularizes the initial singularity by introducing the finite microscopic scale ℓ_*.

4.3. Evolution of $L_p(t)$ and the Law for $c_{\rm eff}(t)$

From Eq. (3) one obtains

$$c_{\rm eff}(t) = \left(\frac{\hbar G}{[L_p(t)]^2}\right)^{1/3} = c_0\left(\frac{L_p(t)}{L_p(t_0)}\right)^{-2/3}. \tag{29}$$

Thus, an *increase* of the effective Planck length $L_p(t)$ with cosmic time corresponds to a *decrease* of the effective signal speed $c_{\rm eff}(t)$. Because $L_p(t)$ is determined by the evolving metric component $G_{ik}(t)$, the apparent variation of $c_{\rm eff}$ reflects purely geometric evolution rather than any change in the fundamental constants $\hbar$, G, or ℓ_*.

Operationally, $c_{\rm eff}(t)$ governs the null–cone for large–scale causal processes (e.g., horizon formation), whereas all local laboratory measurements remain tied to the constant $c_{\rm loc}$ of the metric (5).

Having established the large–scale consequences of the variable geometric scale, we now turn to its microscopic manifestation—the appearance of stable topological defects that correspond to elementary particles.

5. Elementary Particles as Topological Defects

5.1. General Concept

Elementary particles are interpreted as stable, localized defects of spatial connectivity. Each defect corresponds to a continuous field configuration $A_i(x)$ whose topology cannot be removed by smooth deformations of the geometry. The associated topological invariants (winding number, linking class, Hopf index) encode the particle's charge, spin, and baryon number.

 doi:10.20944/preprints202510.1813.v1

5.2. Topological Invariants and Energy Functional

Every finite–energy configuration of the antisymmetric field A_i is characterized by an integer–valued invariant of the form

$$Q_{\text{link}} = \frac{1}{16\pi^2}\int d^3x\,\epsilon^{ijk}A_iF_{jk} = \frac{1}{4\pi^2}\int \mathbf{A}\cdot(\nabla\times\mathbf{A})\,d^3x, \tag{30}$$

which counts the linking of field lines and coincides with the Hopf index H. Here F_{ij} denotes the spatial components of the antisymmetric connectivity tensor introduced in §3.4; in the quasi–isotropic limit $F_{ij}\approx A_{ij}$. Configurations with different Q_{link} cannot be transformed into each other continuously. The field energy

$$E[A_i] = \int d^3x\,\frac{1}{2\mu_0}F_{ij}F^{ij}, \tag{31}$$

has local minima at fixed Q_{link}, providing topological protection of the defect. This mechanism parallels the stability of solitons in the Faddeev–Niemi and Skyrme models [4–6].

5.3. Model Configurations

Stable localized solutions of the energy functional (31) exist for discrete values of the linking number Q_{link}. Below we summarize the lowest–order configurations that correspond to the known elementary fermions.

Electron (toroidal defect).

A single–link ($|Q_{\text{link}}| = 1$) configuration has toroidal symmetry with a stable circulation of $F_{\mu\nu}$. The electric charge e corresponds to the sign of the linking number, and the spin orientation follows from the direction of circulation. The configuration is single–connected under 2π rotations and changes sign under a 2π spatial rotation while returning to itself only after 4π, reproducing the spinor behaviour of a fermion with $s = \frac{1}{2}$.

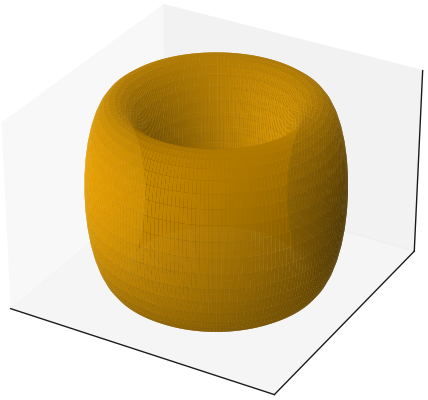

Figure 2. Model configuration of an electron as a toroidal topological defect with $|Q_{\text{link}}| = 1$.

Proton (trefoil–type knot).

A configuration with $|Q_{\text{link}}| = 3$ corresponds to a knotted trefoil structure with three intertwined channels of field circulation. These channels naturally parallel the three color degrees of freedom in QCD, while the total orientation of the flows gives net charge $+e$. The trefoil knot belongs to the C_3 symmetry class: its three equivalent branches provide a natural geometric analogue of the three $SU(3)_{\text{color}}$ channels in quantum chromodynamics.

 doi:10.20944/preprints202510.1813.v1

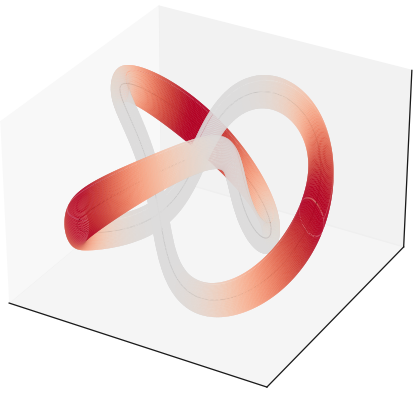

Figure 3. Model configuration of a proton as a trefoil–type knot with $|Q_{\text{link}}| = 3$.

Neutron (balanced knot).

A neutral configuration similar to the proton but with opposite linking in one of the channels, yielding total charge 0. The overall topological class remains the same ($\pi_3(S^3)$ invariant conserved), ensuring baryon number conservation, while the internal orientation of one strand is reversed, producing charge neutrality without altering the total spin orientation. Beta decay corresponds to a local reconnection of field lines,

$$n \;\rightarrow\; p + e^{-} + \bar{\nu}_e,$$

which reduces the net linking number by one unit and emits a leptonic filament representing the antineutrino.

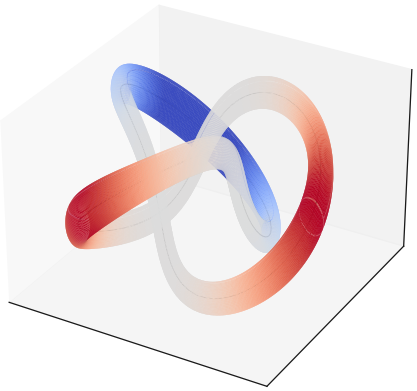

Figure 4. Model configuration of a neutron as a balanced neutral knot.

These configurations form the minimal topological basis of the model; their conserved invariants account for charge, spin, and baryon number, as discussed in the next subsection.

5.4. Physical Properties Derived from Topology

The observable quantum numbers of elementary particles follow directly from the topological invariants of their connectivity configurations. Below we summarize the correspondence between geometric quantities and physical observables.

 doi:10.20944/preprints202510.1813.v1

Charge as winding number.

Electric charge is identified with the integer winding of the $U(1)$ phase ϕ around a closed loop γ in the connectivity domain:

$$Q = ne, \qquad \frac{1}{2\pi}\oint_{\gamma} \nabla\phi \cdot d\ell = n \in \mathbb{Z}. \tag{32}$$

The integer n represents the homotopy class $\pi_1(S^1)$ of the phase map, and the factor e fixes the physical unit of charge by calibration to the electron. Quantization of charge thus follows from the topological quantization of the phase circulation, as in classical soliton models [4,6].

Spin as orientation of circulation.

A toroidal defect admits two stable orientations of phase circulation (clockwise/counter–clockwise). Upon a 2π spatial rotation the configuration changes sign, while a 4π rotation restores identity, reproducing the spinor property of fermions ($s = \frac{1}{2}$) [7]. The two orientations correspond to the double covering $SU(2) \to SO(3)$ of the rotation group, so that the defect's phase field lives on a nontrivial spin bundle over Σ_t.

Stability and mass.

Topological protection ensures stability: a torus or knot cannot be continuously deformed into vacuum without breaking connectivity. The particle mass corresponds to the minimum of the energy functional (31) at fixed Q_{link}. Different topological classes yield different minima, explaining the hierarchy between electron, proton, and neutron masses. The characteristic energy density scales as $E \sim \hbar c_{\text{loc}}/\ell_*$, so that the rest mass $m \sim E/c_{\text{loc}}^2$ provides a natural link between the geometric cutoff ℓ_* and the observed mass spectrum.

Color and baryon number from knot structure.

Trefoil–type defects possess three intertwined branches, naturally associated with three color channels. The conserved baryon number corresponds to the homotopy invariant $\pi_3(S^3)$ characterizing the knot class, analogous to the Skyrme baryon number [4,6]. The integer associated with $\pi_3(S^3)$ measures the degree of the map from physical space to the compactified field space and remains invariant under smooth deformations, ensuring baryon number conservation.

Beta decay as reconnection.

Neutron decay $n \to p + e^- + \bar{\nu}_e$ corresponds to a local reconnection that changes $Q_{\text{link}} \mapsto Q_{\text{link}} - 1$, reducing the total linking by one unit and emitting a leptonic filament representing the antineutrino. Similar reconnection phenomena are observed in knotted field configurations [8–10].

Quantitative estimates.

Experimental bounds on the electron radius $r_e < 10^{-19}\,\text{m}$ imply that the toroidal core of the corresponding defect satisfies $r_{\text{core},e} \lesssim 10^{-19}\,\text{m}$. For the proton, assuming a core radius $r_{\text{core}} \sim 0.25\,\text{fm}$ and total trefoil radius $R \sim 0.8\,\text{fm}$, one obtains an effective charge radius $\sim 0.84\,\text{fm}$, in agreement with experiment. These values make the model quantitatively falsifiable rather than purely qualitative.

These relations demonstrate that the intrinsic quantum numbers of matter arise from purely geometric invariants of space connectivity, providing a direct bridge between topology and particle phenomenology.

Limitations.

The present correspondence between geometric topology and particle physics remains incomplete. In particular, the chiral structure of weak interactions has not yet been derived explicitly, and anomaly–cancellation conditions are not automatically guaranteed by topology alone. Quantitative predictions such as particle masses, mixing angles, and coupling constants require explicit minimization of the

 doi:10.20944/preprints202510.1813.v1

energy functionals for each topological defect. These open issues define natural directions for further development, in line with ongoing studies of topological solitons and knotted field configurations in particle physics.

6. Observable Effects

The framework predicts several potentially observable consequences of metric anisotropy and geometry–dependent effective constants. The most promising channels include gravitational lensing, propagation of gravitational waves, laboratory tests of metric corrections, and cosmological imprints in the early Universe.

Each effect below follows directly from the local anisotropy tensor $\beta_{ik} = G_{ik} - \delta_{ik}$ and the geometry–dependent signal speed $c_{\text{eff}}(x)$, providing experimentally accessible constraints on the underlying geometry.

6.1. Anisotropic Lensing

A directional dependence of the deflection angle in weak fields arises from the anisotropy of the spatial metric $G_{ik} = \delta_{ik} + \beta_{ik}$, where $\operatorname{tr}\beta = 0$. The effective gravitational potential satisfies the Poisson equation $\nabla^2\Phi_{\text{eff}} = 4\pi G\rho(1 + \beta_{ij}\hat{n}^i\hat{n}^j)$, so that the effective mass becomes angle–dependent, $M_{\text{eff}}(\varphi)$. To first order in β_{ik},

$$\hat{\alpha}(\varphi) \simeq \frac{4GM_{\text{eff}}(\varphi)}{c_{\text{eff}}^2 b}\left[1 + \tfrac{1}{2}\,\beta_{ij}\hat{n}^i\hat{n}^j\right], \tag{33}$$

where b is the impact parameter. Observation of direction–dependent deflection would therefore probe the anisotropic components of G_{ik}. For typical weak–lensing angles $\hat{\alpha} \sim 10^{-5}$, an anisotropy $|\beta| \sim 10^{-3}$ would produce a differential deflection $\Delta\hat{\alpha} \sim 10^{-8}$ rad, within reach of next–generation surveys (Euclid, SKA).

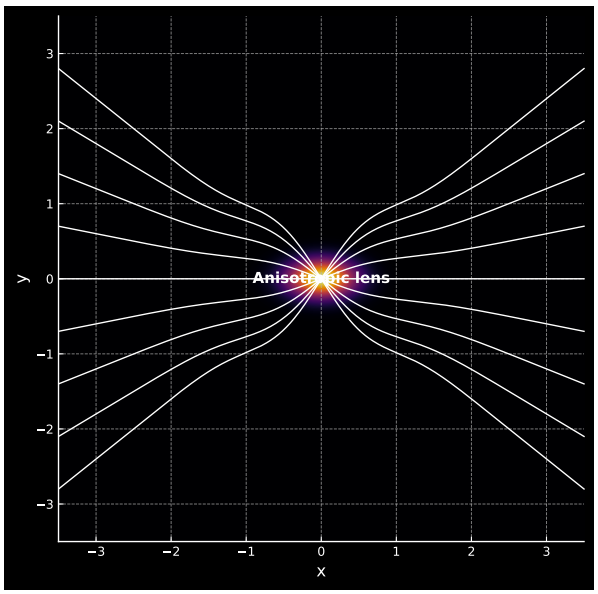

Figure 5. Schematic illustration of anisotropic lensing due to geometric anisotropy of the metric G_{ik}.

6.2. Speed of Gravitational Waves

The effective metric for tensor modes may produce a mild directional dependence of the phase velocity:

$$v_g(\hat{\boldsymbol{n}}) \approx c_{\text{eff}}\,[1 + \delta(\hat{\boldsymbol{n}})], \qquad |\delta| \ll 1, \tag{34}$$

where $\delta(\hat{\boldsymbol{n}}) \simeq \frac{1}{2}\,\beta_{ij}\hat{n}^i\hat{n}^j$ at leading order. The observational bound $|v_g - c_{\text{eff}}|/c_{\text{eff}} \lesssim 10^{-15}$ from GW170817 translates into a constraint on the anisotropy amplitude $|\beta_{ik}| \lesssim 10^{-15}$, confirming that local

 doi:10.20944/preprints202510.1813.v1

Lorentz invariance holds with extremely high precision. Future multi–messenger detections with LISA and pulsar–timing arrays could improve this limit by several orders of magnitude.

6.3. Laboratory Tests

Strong electromagnetic fields can induce minute corrections to the metric via the field stress tensor (17). For a uniform field region, the fractional correction to the metric can be estimated as

$$\frac{\delta g}{g} \sim \frac{E^2 + B^2}{E_{\text{Planck}}^2}, \qquad E_{\text{Planck}} \equiv \frac{c_{\text{loc}}^4}{\sqrt{G}} \approx 1.3 \times 10^{61}\,\text{V/m}, \tag{35}$$

which is exceedingly small ($\sim 10^{-40}$ for laboratory fields with $E, B \sim 10^9$ V/m) but may in principle be enhanced in resonant optical cavities, high–intensity laser systems, or precision interferometric setups where cumulative phase shifts scale with optical path length. A null result at the level of $\delta g/g < 10^{-35}$ would already constrain ℓ_* to be below $\sim 10^{-23}$ m.

6.4. Cosmological Signatures

Temporal variation of the geometry–dependent quantities $L_p(t)$ and $c_{\text{eff}}(t)$ modifies the sound horizon and the growth of super–horizon correlations in the early Universe. Observable consequences include slight shifts in the positions of the acoustic peaks in the CMB spectrum and potential distortions in the stochastic gravitational–wave background, both of which provide quantitative tests of the model. To first order, the fractional shift of the sound horizon obeys

$$\frac{\Delta r_s}{r_s} \simeq -\frac{2}{3}\frac{\Delta c_{\text{eff}}}{c_{\text{eff}}} \approx -\frac{2}{3}\frac{\Delta L_p}{L_p}, \tag{36}$$

implying that a 10^{-3} change in L_p during recombination would shift the first acoustic peak by $\Delta\ell \sim 1$, a level detectable with current CMB precision. Similarly, slow temporal drifts of $c_{\text{eff}}(t)$ alter the transfer function of primordial tensor modes, producing frequency–dependent tilts in the stochastic gravitational–wave background that could be probed by LISA and PTA networks.

Together, these effects translate the purely geometric parameters (ℓ_*, G_{ik}) into observable quantities across a wide range of scales, from tabletop optics to cosmology, offering a falsifiable phenomenology for the unified connectivity framework.

7. Comparison with Current Topological Theories

To place the proposed framework in context, we compare it with the main existing topological and quantum–geometric approaches. The emphasis is on the number of fundamental parameters, the mathematical carriers of topology, and the type of observable predictions.

7.1. Cosmic Defects

The classical Kibble mechanism and the models of Vilenkin and Shellard [11,12] describe the formation of domain walls, strings, and monopoles during phase transitions in the early Universe. Recent PTA results (NANOGrav, EPTA, PPTA) indicate a stochastic gravitational–wave background [13], potentially explainable by cosmic strings [14,15]. In contrast, the present framework treats the defect as the *connectivity geometry itself*, governed by a single fundamental scale ℓ_*. An observational discriminator would be the angular anisotropy of the SGWB in the case of an anisotropic spatial metric G_{ik}. The predicted pattern of multipoles depends on the tensor β_{ik} and may be constrained by future PTA anisotropy measurements.

7.2. Hopfions and Knotted Electromagnetic Fields

Works by Ranada [8], Irvine and Kedia [9], and subsequent reviews [10] demonstrate that Maxwell's equations admit knotted and linked field configurations ("hopfions") classified by the

 doi:10.20944/preprints202510.1813.v1

Hopf index H. In the present model, similar topological structures arise at the level of spatial connectivity rather than within a separate material field. Nevertheless, the same computational tools for evaluating H apply to our particle–like defects (electron, proton, neutron), enabling quantitative analysis of their stability and energy hierarchy. The geometric cutoff ℓ_* plays the role of a natural ultraviolet regulator that replaces the arbitrary core size used in standard hopfion simulations.

7.3. Skyrme Model of Baryons

The Skyrme model [4] and its modern extensions [16,17] describe baryons as topological solitons in nonlinear SU(2) fields, where the baryon number corresponds to a $\pi_3(S^3)$ invariant. In our framework the carrier of topology is the three–dimensional connectivity itself, and the single parameter ℓ_* defines the geometric cutoff scale. This removes the arbitrariness of choosing a specific Lagrangian and facilitates direct comparison with observable quantities such as proton and neutron radii. While Skyrme models contain multiple phenomenological constants (f_π, e_{Sk}, ...), the present construction uses only one universal length ℓ_*, reducing parameter degeneracy while preserving the same topological content.

7.4. Loop Quantum Gravity and Kerr Regularization

Recent results within loop quantum gravity (LQG) [18,19] demonstrate the removal of the Kerr ring singularity and the emergence of a minimal radius. The present model shares similar phenomenology—absence of closed timelike curves, finite $r_{\min}$, and shifts of the ergosphere observable via EHT shadows and GW ringdown spectra. The key distinction is conceptual: in LQG regularization arises from quantization of geometry with several free parameters (e.g. Barbero–Immirzi γ), whereas here it stems from a single geometric–topological scale ℓ_*. This difference yields distinct deformation portraits of the Kerr metric, which can be tested by Bayesian fits to EHT and LIGO/Virgo/KAGRA data. Quantitatively, the expected shift of the photon–ring radius is $\Delta r/r \simeq (\ell_*^2/R_S^2)^{1/3}$, yielding $\Delta r/r \sim 10^{-3}$ for $\ell_* \sim 10^{-22}$ m and a $10\,M_\odot$ black hole—within the reach of next–generation EHT baselines.

7.5. Astrophysical Tests of Kerr

Observations of the M87* and Sgr A* shadows (EHT [20,21]) and of gravitational–wave ringdown spectra (LIGO/Virgo/KAGRA [22]) already provide direct probes of regularized Kerr geometries. Moreover, the constraint on the speed of gravitational waves from GW170817 [23] requires $|c_{\mathrm{gw}} - c|/c \lesssim 10^{-15}$, which the present model satisfies automatically since local Lorentz invariance with fixed c_{loc} is preserved by construction.

Summary of distinctions.

Framework	Carrier of topology	Free parameters	Singularities	Observable tests
GR + EM	metric $g_{\mu\nu}$ + field A_μ	none	yes	lensing, GW speed
Cosmic strings	scalar/gauge fields	tension μ	yes	SGWB anisotropy
Skyrme model	$SU(2)$ field $U(x)$	f_π, e_{Sk}	regular	baryon masses
LQG	spin networks	γ, etc.	regular	BH area spectrum
This work	connectivity tensor G_{ik}	ℓ_*	regular	CMB, EHT, PTA

The comparison shows that the proposed theory retains the minimal set of assumptions while covering both the microscopic (particle) and macroscopic (cosmological and gravitational) domains. Its falsifiability through direct astronomical and laboratory tests distinguishes it from most existing topological approaches.

8. Discussion and Outlook

The proposed axiomatic framework unifies the geometric description of gravity and electromagnetism through the concept of local spatial connectivity. Within this picture, both curvature and

 doi:10.20944/preprints202510.1813.v1

field strength originate from a single tensor G_{ik}, whose symmetric and antisymmetric components represent, respectively, gravitational and electromagnetic sectors. The introduction of one universal scale ℓ_* regularizes classical singularities and provides a geometric origin for quantum phenomena. Future work will refine the operational definition of ℓ_*, extend the classification of topological defects, and provide numerical modeling of the evolution of $L_p(t)$ with confrontation to astrophysical and cosmological data.

Phenomenological constraints.

Precision measurements of the electron $g-2$ and electric dipole moment require any internal structure to appear only above a compositeness scale $\Lambda \gtrsim 10^{20}\,\mathrm{m}^{-1} \sim 10\,\mathrm{TeV}$. The present construction is consistent with these limits, since the characteristic core size of the electron defect is expected to satisfy $r_{\mathrm{core},e} \ll \Lambda^{-1} \sim 10^{-20}\,\mathrm{m}$. Astrophysical tests from EHT shadows and gravitational–wave ringdown spectra further restrict the geometric scale to $\ell_* \lesssim 10^{-22}$–$10^{-23}\,\mathrm{m}$, consistent with the absence of measurable deviations from general relativity.

Future directions.

Promising extensions of the framework include:

(i) numerical minimization of toroidal and knotted configurations to estimate corresponding particle masses and magnetic moments;
(ii) explicit treatment of chirality and weak interactions within the connectivity picture;
(iii) confrontation with observational signatures such as particle charge radii, anisotropic gravitational lensing by macroscopic defects, and the angular structure of the SGWB;
(iv) exploration of links with quantum–information geometry and Fisher–based formulations of quantum mechanics, which may provide an alternative derivation of the quantum potential at the scale ℓ_*;
(v) development of an effective Lagrangian for G_{ik} to connect the present axiomatic model with covariant field theory.

Concluding remark.

Overall, the theory provides a unified geometric language linking gravity, electromagnetism, and quantum structure, while remaining directly testable through cosmological and astrophysical observations. By reducing the number of postulates to a single fundamental scale ℓ_*, it opens a route toward a falsifiable and minimal unification scheme where topology, geometry, and dynamics emerge from one underlying principle.

Funding: This research received no external funding.

Acknowledgments: The author thanks colleagues for discussions and constructive comments.

References

1. Polchinski, J. *String Theory. Vols. 1–2*; Cambridge University Press, 1998.
2. Rovelli, C. *Quantum Gravity*; Cambridge University Press, 2004.
3. Ashtekar, A.; Lewandowski, J. Background Independent Quantum Gravity: A Status Report. *Classical and Quantum Gravity* **2004**, *21*, R53–R152, [gr-qc/0404018]. https://doi.org/10.1088/0264-9381/21/15/R01.
4. Skyrme, T.H.R. A Non-Linear Field Theory. *Proceedings of the Royal Society A* **1961**, *260*, 127–138. https://doi.org/10.1098/rspa.1961.0018.
5. Faddeev, L.D.; Niemi, A.J. Stable knot-like structures in classical field theory. *Nature* **1997**, *387*, 58–61. https://doi.org/10.1038/387058a0.
6. Manton, N.; Sutcliffe, P. *Topological Solitons*; Cambridge University Press, 2004. https://doi.org/10.1017/CBO9780511617034.
7. Wilczek, F.; Zee, A. Linking Numbers, Spin, and Statistics of Solitons. *Physical Review Letters* **1983**, *51*, 2250–2252. https://doi.org/10.1103/PhysRevLett.51.2250.

 doi:10.20944/preprints202510.1813.v1

8. Rañada, A.F. A Topological Theory of the Electromagnetic Field. *Letters in Mathematical Physics* **1989**, *18*, 97–106. https://doi.org/10.1007/BF00401864.
9. Kedia, H.; Bialynicki-Birula, I.; Peralta-Salas, D.; Irvine, W.T.M. Tying Knots in Light Fields. *Physical Review Letters* **2013**, *111*, 150404, [1302.0342]. https://doi.org/10.1103/PhysRevLett.111.150404.
10. Guslienko, K.Y. Magnetic Hopfions: A Review. *Magnetism* **2024**, *4*, 383–399. https://doi.org/10.3390/magnetism4040025.
11. Kibble, T.W.B. Topology of Cosmic Domains and Strings. *Journal of Physics A: Mathematical and General* **1976**, *9*, 1387–1398. https://doi.org/10.1088/0305-4470/9/8/029.
12. Vilenkin, A.; Shellard, E.P.S. *Cosmic Strings and Other Topological Defects*; Cambridge University Press, 1994.
13. Agazie, G.; et al. The NANOGrav 15-year Data Set: Evidence for a Gravitational-Wave Background. *The Astrophysical Journal Letters* **2023**, *951*, L8, [2306.16213]. https://doi.org/10.3847/2041-8213/acdac6.
14. Auclair, P.; Ringeval, C.; Sakellariadou, M.; Steer, D.A. Probing the gravitational wave background from cosmic strings with LISA. *Journal of Cosmology and Astroparticle Physics* **2019**, *2019*, 030, [1909.00819]. https://doi.org/10.1088/1475-7516/2019/09/030.
15. LISA Consortium. Laser Interferometer Space Antenna: Science Requirements and Mission Status, 2024.
16. Beznogov, M.V.; Raduta, A.R. Bayesian Survey of the Dense Matter Equation of State built upon Skyrme effective interactions, 2023, [2308.15351]. arXiv preprint.
17. Beznogov, M.V.; Raduta, A.R. Bayesian inference of the dense matter equation of state built upon extended Skyrme interactions. *arXiv preprint* **2024**, [2403.19325].
18. Fazzini, F.; Husain, V.; Wilson-Ewing, E. Shell-crossings and shock formation during gravitational collapse in effective loop quantum gravity. *Physical Review D* **2024**, *109*, 084032, [2312.02032]. https://doi.org/10.1103/PhysRevD.109.084032.
19. Fazzini, F. Non-uniqueness of the shockwave dynamics in effective loop quantum gravity. *arXiv preprint* **2025**, [2502.03003].
20. Event Horizon Telescope Collaboration. First M87 Event Horizon Telescope Results. I. The Shadow of the Supermassive Black Hole. *The Astrophysical Journal Letters* **2019**, *875*, L1. https://doi.org/10.3847/2041-8213/ab0ec7.
21. Event Horizon Telescope Collaboration. First Sagittarius A* Event Horizon Telescope Results. I. The Shadow of the Supermassive Black Hole in the Center of the Milky Way. *The Astrophysical Journal Letters* **2022**, *930*, L12. https://doi.org/10.3847/2041-8213/ac6674.
22. LIGO Scientific Collaboration and Virgo Collaboration and KAGRA Collaboration. Tests of General Relativity with GWTC-3 and implications for ringdown spectroscopy. *Physical Review D* **2022**, *106*, 104042. https://doi.org/10.1103/PhysRevD.106.104042.
23. Abbott, B.P.; et al. Gravitational Waves and Gamma-Rays from a Binary Neutron Star Merger: GW170817 and GRB 170817A. *The Astrophysical Journal Letters* **2017**, *848*, L13. https://doi.org/10.3847/2041-8213/aa920c.